Time-dependent annealing and deposition on substrates with repulsive interactions

J. A. Venables,[1,2,*] J. DeGraffenreid,[1] D. Kay,[2] and P. Yang[1]
[1]*Department of Physics, Arizona State University, Tempe, Arizona 85287-1504, USA*
[2]*School of Science and Technology, University of Sussex, Brighton, United Kingdom*
(Received 12 February 2006; revised manuscript received 21 June 2006; published 9 August 2006)

In models of nucleation and growth of crystals on surfaces, it is often assumed that the energy surface of the substrate is flat, that diffusion is isotropic, and that capture numbers can be calculated in the diffusion-controlled limit. We lift these restrictions and formulate the general time-dependent problem in a two-dimensional (2D) potential field. We utilize the master equation discretization (MED) method to solve the 2D time-dependent diffusion field of adparticles on general nonuniform (rectangular grid) substrates, and compare it against competing algorithms, including the fast Fourier transform (FFT) and hybrid-FFT methods previously introduced, for periodic boundary conditions. The physical context is set by the importance of repulsive interactions in the nucleation and growth of many nanostructures, e.g., metal nanoclusters, hut clusters, and nanowires. The programs, realized in MATLAB®6.5, are used to obtain quantitative capture numbers, aspect and direct impingement ratios, and other island growth quantities in the presence of potential fields, when particular surface processes are included. The case of no corner rounding is studied in detail. Strongly anisotropic potentials favor wire growth, which can be considerably influenced by alternate deposition and annealing, and the location of neighboring islands. Physical examples are given based on Ge/Si(001) material parameters. Essentially similar programs, differing only in outputs, are used to visualize the diffusion field and to produce realistic movies of crystal growth. Examples given here are linear deterministic calculations, but the framework allows for inclusion of nonlinear and statistical effects for particular applications.

DOI: 10.1103/PhysRevB.74.075412 PACS number(s): 68.55.Ac, 81.10.Aj, 81.15.Kk, 02.30.Jr

I. INTRODUCTION

Diffusion and capture processes involved in nucleation and growth on surfaces have received widespread attention over many years.[1,2] More recently, scanning tunneling microscopy (STM) and field ion microscopy (FIM) experiments have been able to follow atomic-level events, and to measure energies for individual activated processes. Over the last few years, it has become clear that capture of adparticles cannot always be treated in the diffusion-controlled limit, and that adparticle interactions are often important in forming nanostructures. Analyses have been presented of low-temperature STM data on close-packed metal surfaces,[3–5] in which repulsive interactions, between diffusing adatoms and other adatoms and clusters, causes capture rates to be reduced, sometimes substantially.[6,7] Similarly, Ge/Si(001) hut cluster and metal silicide growth involve repulsive interactions. Progress in the quantitative description of the early stages of growth has been reviewed,[7,8] where more background information and references can be found.

In this paper, we calculate and visualize the diffusion field of adparticles around growing clusters, and derive capture numbers and other quantitative data for several potentials, extending previous conference papers.[9,10] We first recap, in Sec. II and Appendix A, the analytic formulation of diffusion and capture on a substrate with a nonuniform potential for diffusing adparticles. This potential is defined with respect to an origin on the two-dimensional (2D) substrate, and so is written $V(\boldsymbol{r})$. The object at the origin can be a cluster, a defect site, or another (diffusing) adparticle. Solutions for radial symmetric potentials have already been reported,[6,7] and some further comments are made here. In Appendix B we describe our procedure[9] to obtain time-dependent field and capture number solutions with anisotropic diffusion using a fast Fourier transform (FFT) method.

In Secs. III and IV, we adapt the master equation discretization (MED) algorithm[11] to show how repulsive interactions slow the growth of 2D quasirectangular clusters arranged on a lattice. The MED algorithm accurately incorporates the underlying dynamics of diffusion and drift on a lattice in a general potential field; we compare this algorithm with others in Appendix C. The case of rectangular clusters, with restricted corner diffusion during annealing, both with and without repulsive interactions, is examined quantitatively.

We then extend these same methods in Secs. V and VI to the general case where deposition, growth, and/or annealing occur simultaneously, and discuss the role of nucleation in relation to growth at nanometer scales, for the specific cases of Ge/Si(001) and silicide wire growth. The programs are coded in MATLAB®6.5, and produce quantitative results, in particular anisotropic capture numbers and graphic output. The programs enable one to visualize the diffusion field, and the growth of individual crystals, when particular surface processes are included. This output can be viewed conveniently in the form of MATLAB® movies, which are realistic and fast enough for real-time conference presentation using a modern laptop computer. To conclude, we summarize the physical insight gained, and outline some future developments, including combined nucleation and growth, and other nonlinear and statistical behavior.

II. DIFFUSION IN 2D POTENTIAL FIELDS: ANALYTIC FORMULATION

We are interested in solutions of a 2D diffusion equation for the adparticle concentration $c(\boldsymbol{r},t)$, when there may be

sources and sinks at various positions. The simplest case to think about is when we have a loss term governed by a characteristic mean lifetime τ. The governing partial differential equation (PDE) is then

$$\partial c(\boldsymbol{r})/\partial t = G - c(\boldsymbol{r})/\tau - \boldsymbol{\nabla}\cdot\boldsymbol{j}(\boldsymbol{r}), \tag{1}$$

where $\boldsymbol{j}(\boldsymbol{r})$ is the diffusive flux at position $\boldsymbol{r}$. In the epitaxial growth literature,[1,2,7,8] the source term G is equal to the deposition flux F during deposition and is typically zero during annealing and the adparticle concentration may be variously described as c, n, or n_1.

In the absence of a potential field, the flux term $\boldsymbol{j}(\boldsymbol{r})$ is defined as $-D\boldsymbol{\nabla}c(\boldsymbol{r})$, where D is the *chemical* diffusion constant. Thus the last term in Eq. (1) is equal to $D\nabla^2 c(\boldsymbol{r})$ if D is indeed constant; but on an anisotropic substrate, the general form of D is a second rank tensor, and there is no absolute reason for D to be independent of position or of time. Equation (1) has been solved for constant D in various approximations to determine the growth rate of clusters by capture of adparticles on surfaces. The case when τ is finite (i.e., $\tau^{-1}>0$) is a general way of introducing competing loss processes, such as re-evaporation, or capture by other clusters, in the uniform depletion or mean-field approximation.[1,7,12,13]

The other limiting possibility is to omit this term (i.e., $\tau^{-1}=0$), but to arrange the clusters on a lattice and use appropriate boundary conditions. This *lattice* approximation[1] to capture numbers was developed for radial symmetry by Halpern,[14] Stowell,[15] Lewis[16] and others. The search for realistic intermediate expressions, taking into account cluster sizes and positions during deposition or annealing, is an ongoing research problem that has been reviewed[8] but is not pursued further here. Rather, we place the clusters on a lattice, such as may be appropriate for directed nucleation on a rectangular array of defects, and solve the full time-dependent capture problem with 2D-periodic boundary conditions.

Diffusion in a potential field obeys the Nernst-Einstein equation,[17] and the resulting advection-diffusion equations for the adparticle concentration show, in general, both diffusion and drift.[11] We show that previous results in the 2D nucleation and growth literature[6,7] correspond to this type of equation and solutions. With nonzero $V(\boldsymbol{r})$ we need to evaluate the response to concentration $[\boldsymbol{\nabla}c(\boldsymbol{r})]$ and potential $[\boldsymbol{\nabla}V(\boldsymbol{r})]$ gradients, via consideration of phenomenological transport coefficients, which leads to a more general definition of $\boldsymbol{j}(\boldsymbol{r})$ in terms of the gradient of the chemical potential $\boldsymbol{\nabla}\mu(\boldsymbol{r})$. This definition can be written in terms of either D, the chemical, or D^*, the tracer, diffusion coefficient. Under certain reasonable conditions,[7,17] $(D/D^*)=\beta\{\delta\mu/\delta[\ln(c)]\}$. The simplest expression for $\boldsymbol{j}(\boldsymbol{r})$, using this ratio, is

$$\boldsymbol{j}(\boldsymbol{r}) = -(D^* c)\beta\boldsymbol{\nabla}\mu. \tag{2}$$

We now need the expression for $\mu(\boldsymbol{r})$ for a nonideal adsorbed gas of adparticles, which is $\mu(\boldsymbol{r})=\mu_0+V(\boldsymbol{r})+\beta^{-1}\ln(\gamma c)$, where γ is the activity. For this form of $\mu(\boldsymbol{r})$, the original definition of $\boldsymbol{j}(\boldsymbol{r})$ can be written as[7]

$$\boldsymbol{j}(\boldsymbol{r}) = -(Dc)\{1+\delta\ln(\gamma)/\delta[\ln(c)]\}^{-1}\beta\boldsymbol{\nabla}\mu; \tag{3}$$

$\{1+\delta\ln(\gamma)/\delta[\ln(c)]\}$ is called the thermodynamic factor. Thus from these equations we find that

$$\boldsymbol{j}(\boldsymbol{r}) = -D\boldsymbol{\nabla}c(\boldsymbol{r}) - [c(\boldsymbol{r})D^*]\beta\boldsymbol{\nabla}V(\boldsymbol{r}). \tag{4}$$

The derivative of $\gamma(\boldsymbol{r})$ is needed to obtain D in the first term in Eq. (4), but D^* remains in the second term. In particular, we are concerned here with solving the capture problem for reasonable forms of the dimensionless potential $\beta V(\boldsymbol{r})$, for example due to adatom-adatom, and/or adatom-cluster repulsion. Using Eq. (4), Eq. (1) becomes

$$\partial c(\boldsymbol{r})/\partial t = G - c(\boldsymbol{r})/\tau + \boldsymbol{\nabla}\cdot[D\boldsymbol{\nabla}c(\boldsymbol{r})] + \boldsymbol{\nabla}\cdot\{[c(\boldsymbol{r})D^*]\beta\boldsymbol{\nabla}V(\boldsymbol{r})\}. \tag{5}$$

Note that although the $\boldsymbol{r}$ dependence is written out explicitly for c and V and there is an implied time dependence, the "constants" G, τ, D, and D^* may also be functions of position (e.g., via concentration or a diffusion energy), or in the cases of G, τ, of time (e.g., during deposition or annealing), without changing Eq. (5).

This paper is concerned with solving Eq. (5) on a rectangular grid, where there may be (repulsive) potential fields present, and providing physical examples where the solutions are useful. There are no analytic solutions for the general form of Eq. (5), even in radial geometry. However, if we assume $\gamma(\boldsymbol{r})=\gamma$ in the model, the thermodynamic factor is unity, so that D and D^* are the same. In this low concentration limit, where $D=D^*=D_1$, the last term of Eq. (5) is given by

$$\boldsymbol{\nabla}\cdot\{[c(\boldsymbol{r})D^*]\beta\boldsymbol{\nabla}V(\boldsymbol{r})\} = D_1\boldsymbol{\nabla}\{c(\boldsymbol{r})\cdot\boldsymbol{\nabla}[\beta V(\boldsymbol{r})]\}, \tag{6}$$

where $\beta=(kT)^{-1}$ makes the variable $\beta V(\boldsymbol{r})$ dimensionless. This restriction to low concentration is not a requirement, but is made here to ensure linearity. The more general case is outlined in Appendix A. These extra terms mean that Eq. (5) is a type of advection-diffusion equation, in which diffusion coexists with drift along concentration and potential gradients. Depending on the model details, we may wish to consider fixed or moving boundary conditions.

III. DISCRETIZATION OF ADVECTION-DIFFUSION EQUATIONS

The numerical solution of advection-diffusion equations (ADEs) has a long history, but recently a new algorithm has been developed that is very efficient in solving equations of this type. Grima and Newman[11] considered ADEs of the general form

$$\partial c(\boldsymbol{r})/\partial t = \boldsymbol{\nabla}\cdot[D\boldsymbol{\nabla}c(\boldsymbol{r})] - \boldsymbol{\nabla}\cdot[c(\boldsymbol{r})\boldsymbol{v}(\boldsymbol{r})], \tag{7}$$

where the velocity field $\boldsymbol{v}(\boldsymbol{r})$ can depend on the concentration $c(\boldsymbol{r})$. The velocity field can be specialized to be proportional to a potential gradient as $\boldsymbol{v}(\boldsymbol{r})=-\alpha\boldsymbol{\nabla}V(\boldsymbol{r})$.[18] With this constraint, the last term of Eq. (7) corresponds exactly to Eq. (6) with $D_1=\alpha/\beta$.

The main algorithm proposed in Ref. 11 was called master equation discretization (MED). It is based on an exact trans-

formation that turns Eq. (7), via two Laplacians, into the form of a master equation. Equation (7) can be shown to be equivalent to

$$\partial c(\boldsymbol{r})/\partial t = D_1\{(E^{-1})\nabla^2[c(\boldsymbol{r})E] - [c(\boldsymbol{r})E]\nabla^2(E^{-1})\}, \quad (8)$$

in our notation, where $E=\exp[\eta V(\boldsymbol{r})]$ and $\eta=\alpha/2D_1$. Since, for our application, we have shown that $D_1=\alpha/\beta$, the exponential involved in the transformation is $E=\exp[\beta V(\boldsymbol{r})/2]$.

The discretization of Eq. (8) is especially simple because the Laplacians can be expressed as sums of the relevant quantities over neighboring lattice points on a grid. This results in the MED for the grid point concentration c_i in the form

$$\partial c_i/\partial t = \sum_j [W_{j\to i}c_j - W_{i\to j}c_i], \quad (9)$$

where in the special case we are considering, the transition probabilities or hopping rates $W_{i\to j}$ are given on a lattice of size a, for nearest neighbors (i and j) only, by

$$W_{i\to j} = (D_1/a^2)\exp[\beta(V_i - V_j)/2]. \quad (10)$$

Computationally, the MED method is powerful because it avoids linearization of the drift terms in Eq. (7), allowing one to use larger space steps than otherwise.[11] The results presented here are based on this MED algorithm. This method satisfies the particle conservation sum rule for all potentials; it is not unconditionally stable, but is accurate and fast enough for the production of MATLAB® movies suitable for real-time presentation, and it works well for very high Peclet numbers. We also introduce a hybrid-FFT procedure, identical in principle to the MED method, which is highly stable and fast for all reasonable time steps.[19] FFT, real space MED, hybrid-FFT and implicit methods are described and compared in Appendixes B and C.

IV. CAPTURE NUMBERS IN RADIAL AND RECTANGULAR GEOMETRY

A. Radial potential models

Two modeling papers have been published on the effect of radial repulsive potential fields on capture numbers in the context of nucleation and growth on surfaces.[6,7] In the first, Ovesson[6] used a 2D square lattice and argued on physical grounds that the energy of each diffusive jump, the transition state energy, would be augmented by half the potential energy difference between the final and the initial sites. In our notation, the diffusion constant for transitions between sites i and j was modified from D_1 to $D_1(\exp\{\beta[V(\boldsymbol{r}_i)-V(\boldsymbol{r}_j)]/2)\}$. The continuum limit was taken, and then this model was applied with radial symmetry. He showed that the effect was the same as replacing the term $\nabla^2[c(r)]$ in the usual radial diffusion equation by $\nabla^2[c(r)]+\nabla[\beta V(r)]\cdot\nabla c(r) + c(r)\nabla^2[\beta V(r)]$. These two terms are the same as those appearing in Eq. (5), if $D=D^*$, and can therefore be lumped together as $\nabla\{c(r)\cdot\nabla[\beta V(r)]\}$, i.e., just as Eq. (6), but limited to radial geometry. Ovesson[6] used his procedure to calculate mean field nucleation densities with a specific form of $V(r)$, constructed to mirror low-temperature STM data on close-packed metal surfaces.[3–5]

Venables and Brune[7] developed a continuum approach based on Eqs. (4) and (5), again in radial geometry, and obtained mean field capture numbers, which can be exponentially reduced when $\beta V(r)$ is substantial. Ovesson[6] did not give explicit values of the capture numbers, but did calculate the increased nucleation density that results at long times from the repulsive potential field. An intriguing point is that Ovesson[6] and Grima and Newman[11] have studied the same problem from opposite ends. Grima and Newman started from the general continuum equation (7), and showed that their MED not only embodies the microscopic dynamics, but is also a very efficient numerical method of solving this whole class of problems. The present discussion shows that, for constant diffusion constants, the two approaches are completely equivalent for radial geometry, and we can represent the general case concisely by Eq. (8). But the approach of Ref. 11 used here is much more general, and will work in any geometry; thus we can proceed with confidence into new areas. The use of the MED algorithm when the diffusion coefficient varies with position (including via strain) is discussed in a companion paper;[20] here the numerical examples are all for spatially homogeneous D_x and D_y.

B. Rectangular line-by-line models without corner rounding

Here, we show that time-dependent capture numbers can be calculated for rectangular geometry with general repulsive potentials $V(\boldsymbol{r})$; in this section we use this example to illustrate the reduction in capture numbers during annealing of a previously deposited adparticle field. The capture numbers can be compared directly with figures for zero potential calculated using the FFT method published in Ref. 9. These numerical methods are given in Appendixes B and C. If Ref. 9 is not familiar it may be helpful to read Appendix B before proceeding further; in particular, the examples given in this section employ the "line by line" method of updating the island size, as shown in Fig. 9(b). This method gives rise to "spikes" in capture number plots, corresponding to the amount of growth that occurs when the island boundary is updated. The size and position of the spikes are very useful markers to track when the x and y edges move. They also enable sensitive tests of the changes that result from different algorithms, or the same algorithms with different integration parameters, as set out in Appendix C.

Figure 1(a) shows the concentration profile which is initially in equilibrium under a 2D anisotropic Gaussian repulsive potential, with maximum value of $\beta V(\boldsymbol{r})$, $\beta V_m=2.5$. At the center of the field an island (size 5×11) is introduced at $t=0$ that acts as a sink. For these examples, we explore moderate anisotropy, with $D_x=5$ and $D_y=10$, such that the r.m.s. diffusion distance $r_d=[2(D_x+D_y)t]^{0.5}$ for the final value of $t=90$ gives $r_d=52$. Thus on a 64×64 mesh, we explore the transition from a completely isolated sink (for $r_d\ll32$ initially) to a relatively strongly coupled array of (nine) sinks (for $r_d>32$ finally), as indicated schematically in Fig. 8(a). In Figs. 1 and 2, the adparticles join each side separately, and corner rounding is not allowed.

The MED capture numbers shown in Fig. 1(b) for $t>0$ have strongly reduced values relative to the case of zero

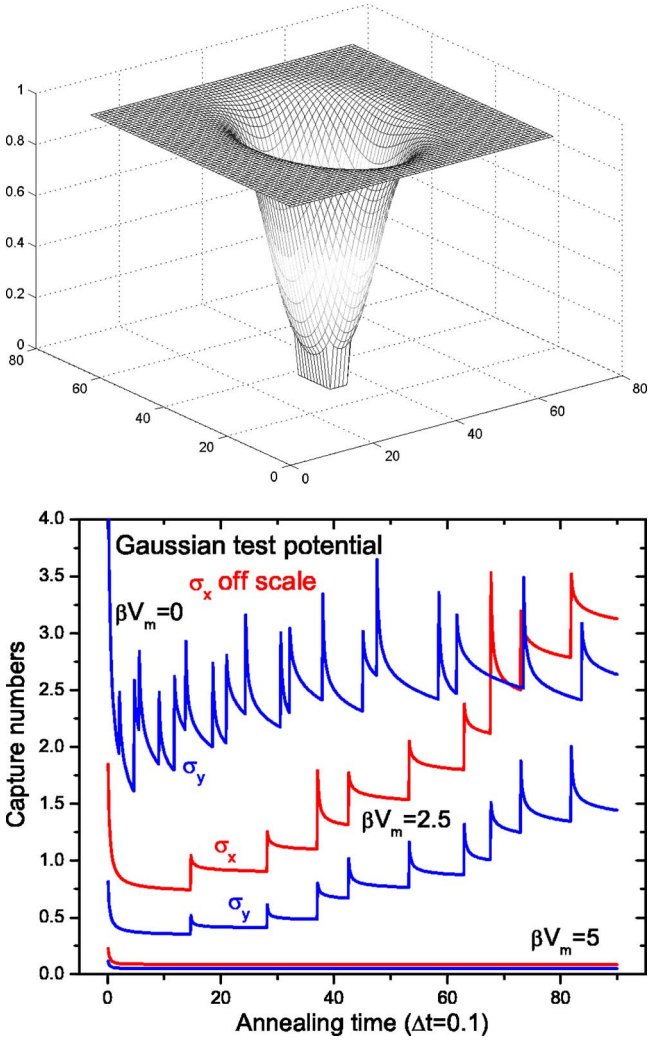

FIG. 1. (Color online) (a) Concentration profile, initially in equilibrium under a Gaussian test potential. (b) Capture numbers σ_x (upper curves, red online) and σ_y (lower curves, blue online) for an initial 5×11 rectangular island (height $h=5$), and $\beta V_m=0$, 2.5 and 5 (after Ref. 9). This figure can be compared with Ref. 9, Fig. 5(b) for $V(\boldsymbol{r})=0$, reproduced here as Fig. 10(b). See text for discussion.

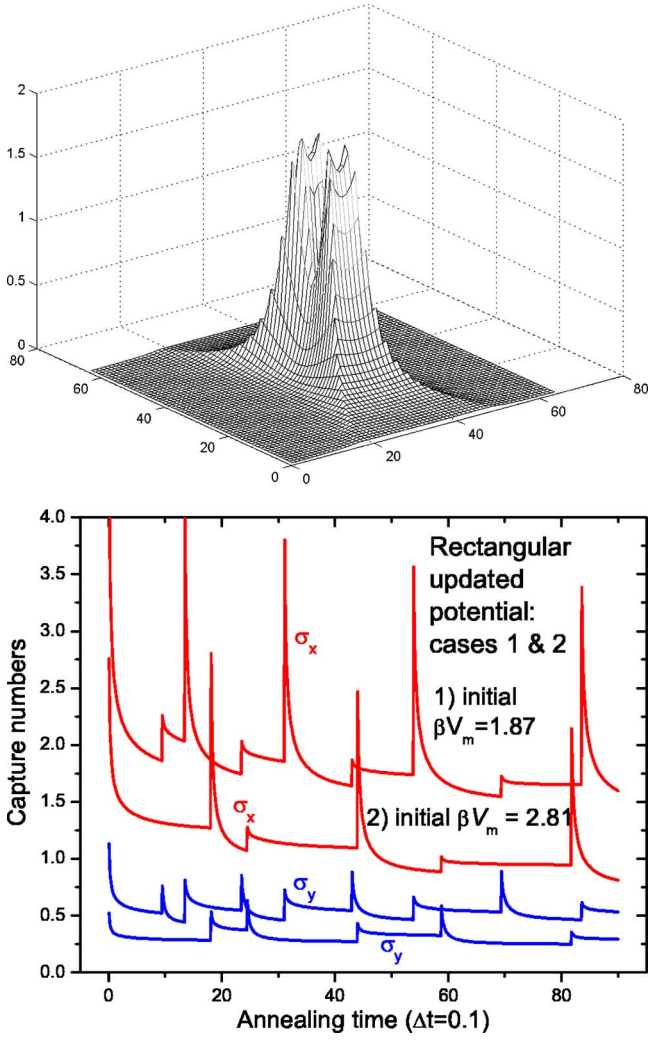

FIG. 2. (Color online) (a) Rectangular potential with initial maximum $\beta V_m=2.32$ at the edge of the 5×11 island. This illustrative potential increases linearly with radial distance r inside the island, and decreases as r^{-3} outside the island with a maxima at the edge of the island. (b) Capture numbers σ_x (upper curves, red online) and σ_y (lower curves, blue online) with no corner crossing, for two similar potentials [$\beta V_m=1.87$ (upper curves) and 2.81 (lower curves)] as a function of annealing time, starting from the equilibrium distribution. Note that the potential is recalculated every time the island size changes.

potential. The case for $\beta V_m=2.5$ shows the capture numbers start low, but increase as the island size increases during annealing. This happens because the repulsive potential is fixed, and so the island eventually outgrows the range of the potential. The absence of spikes in the curves for $\beta V_m=5$ means that essentially no growth occurred during the whole period to $t=90$. These curves can be directly compared with Ref. 9, Fig. 5(b) for $V(\boldsymbol{r})=0$, repeated in Appendix B as Fig. 10(b); the concentration profile is shown as Fig. 10(a).

Figure 2(a) shows a rectangular potential approximating to the strain distribution around a rectangular island, initial size 5×11. This particular potential follows the form used by Ovesson[6] for adparticle elastic interactions, but with the constant B in his Eq. 16 chosen to give maximum repulsive potential at the edge of the island, no matter what size or shape. Here the potential is much "rougher" and more anisotropic, leading to a more challenging test of the numerical methods. For the real space MED method, the sum rules are exactly satisfied as in Fig. 1, but there is a larger ratio of drift to diffusion terms at the edge of the island. The corresponding MED capture numbers are shown in Fig. 2(b) for $\beta V_m=1.87$ and 2.81. Physically, we notice that the capture number stays low, because as the island size is updated, the potential field gets stronger, in contrast to Fig. 1, where it effectively weakens. This situation is more realistic for strained epitaxial islands, e.g., for Ge/Si(001), as discussed in Sec. VI.

The grid Peclet number P_e which measures the relative importance of drift and diffusion over a single mesh element,[11] is just the argument of the exponential in Eq. (10), namely, $\beta(V_i-V_j)/2$. Figure 2(b), with the initial value of $\beta V_m=2.81$, corresponds to a maximum $P_e=0.61$ at the island

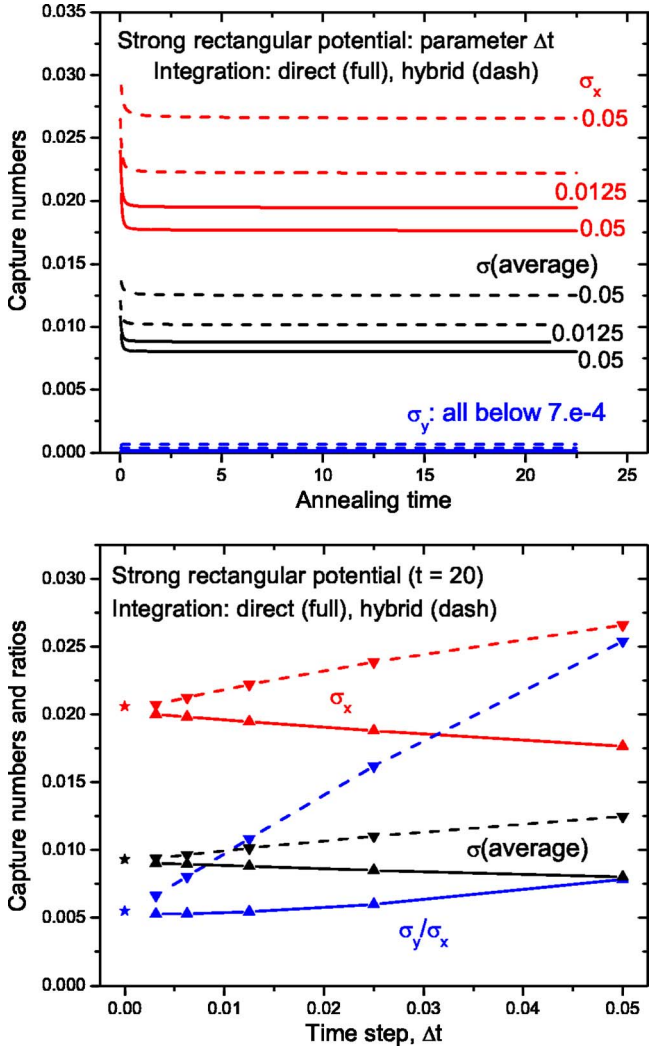

FIG. 3. (Color online) (a) Capture numbers for a strong rectangular potential with maximum $\beta V_m=12.4$, at the edge of the 5×11 island. The values of capture numbers σ_x (upper curves, red online) and σ_y (lower curves, blue online) and the weighted average value (central black lines), as a function of annealing time for two MED integration schemes, direct (full lines) and hybrid-FFT (dashed lines), with the time step, Δt as the parameter. Note that the island size does not change for such a high barrier, even for much longer times. (b) Time-convergence characteristics for these two schemes at a given time ($t=20$), showing σ_x (upper curves, red online), the ratio (σ_y/σ_x) (lower curves, blue online), and the weighted average value (central black lines). Note the superiority of the direct MED scheme at high Peclet numbers (here maximum $P_e=2.85$), and the fact that the two schemes closely approach the analytic barrier capture number (stars) at $\Delta t=0$. See text for discussion.

edge, dropping slightly as the island gets larger. The high accuracy and stability of the MED algorithm has been checked by repeating the calculation with increasing values of βV_m, leading to $P_e\sim3$ being fully stable for quite large time steps $\Delta t=0.05$, as shown in Fig. 3 where $\beta V_m=13.4$. Notably, this range of Peclet numbers is relevant for comparison with epitaxial deposition and annealing experiments. An interesting point is that the real space MED and the hybrid FFT give slightly different answers for high P_e values, as shown in Fig. 3(b). A log-log plot of σ_x values indicates that the hybrid FFT approaches the common solution roughly linearly as the time step is decreased, whereas the real space MED approaches with a somewhat lower power law ~0.85. However, we can see that the latter method is more accurate over the range of Δt studied. In this limit the capture numbers are all very small, namely, diffusive capture is almost entirely suppressed. Note, however, this does not mean that diffusion is suppressed, quite the contrary; it is very rapid, but very few diffusion steps result in capture. This means that other effects may become more important; we return to this case in Secs. V and VI.

Further work is in progress to calculate accurate potentials for real materials and to incorporate such potentials into realistic simulations. However, here we can note some general features of annealing with repulsive potential fields from Figs. 1–3, in comparison with previous work using radial geometry. Venables and Brune[7] calculated capture numbers for various values of βV_m, and found that the capture number expression could be initially approximated by $2\pi(r_k+r_0)\exp(-\beta V_m)$ when $\beta V_m\gg1$, where the factor $2\pi(r_k+r_0)$ represents the number of edge sites just outside the island. The number of edge sites just outside a rectangular 5×11 island with area 55 units is of order 32. Thus the sum of capture numbers $(\sigma_x+\sigma_y)$ for the cases illustrated in Fig. 1(b) would be ~2.63 for $\beta V_m=2.5$ and ~0.216 for $\beta V_m=5$; the corresponding values for Fig. 2(b) are 4.93 for $\beta V_m=1.87$ and 1.93 for $\beta V_m=2.81$. These values correspond to points on the initial rapid drop in the graphs of σ_x and σ_y. This shows that, with the possible exception of the $\beta V_m=5$ curve, the barrier capture numbers represent an upper limit to the long time behavior, as the diffusion zone around the island sink is established.

The capture numbers for the anisotropic rectangular case with strongly varying βV_m around the island edge can make the comparison even closer for Fig. 3. The true solution for high potentials can be estimated quite accurately as the barrier limited capture numbers[7] for x and y edges. In our computation, these are simply the sum of the exponentially weighted barrier heights, namely,

$$\sigma_x=\sum\exp(-\beta V_e), \tag{11}$$

where the sum is taken over the edge elements (V_e) of the potential just outside the island that contribute to σ_x, and similarly for σ_y. This formula has been checked explicitly for the case shown in Fig. 3(b); from Eq. (11) we find $\sigma_x=0.0206$, $\sigma_y=1.14.10^{-4}$, and $(\sigma_y/\sigma_x)=0.0055$, very close to the computed values in the limit of small time steps. For a high barrier, the diffusion gradient is very small, and capture is just determined by the small probability of adparticles being present at the top of the barrier, as emphasized previously (Ref. 7, especially Appendix B). Note that the ratio (σ_y/σ_x) is particularly sensitive to the time step for the hybrid method, when the ratio is small as in this case; this is because the hybrid scheme is better suited for small P_e values, when diffusion is dominant. The opposite is the case at the top of a strong barrier.

C. Rectangular pixel by pixel models with and without corner rounding

In the previous subsections, we have demonstrated pixel by pixel updating of images, but the diffusion calculations were updated line by line. This procedure is good for visualization and for pedagogy, but the capture numbers cannot be as accurately modeled as in a pixel-based computation. It is of course well known that the growing shape of an island depends on the extent of surface diffusion round the island edge; continuum classical crystal growth models deal with the competition between equilibrium and growth forms, Mullins-Sekerka instabilities and dendritic growth, amongst other phenomena. The extreme case of atomistic dendritic growth is diffusion limited aggregation (DLA),[21] and some experimental examples approach this limit. The shapes of 2D islands have been extensively studied, both experimentally and theoretically, particularly in triangular geometry.[2,5,22]

Once again, we can see that the problem as posed can readily bifurcate, and get out of hand. For this initial example, we address the same problem as the last section, and restrain all the "pixel activity" to the edge layer immediate surrounding the rectangular island. Here there are two reasonable limits: the first is no corner rounding as in the previous sections, which makes the shape of the resulting island most anisotropic.

Figure 4(a) shows the capture number results of a pixel calculation with no corner rounding, for the case of no repulsive potential, $V(\boldsymbol{r})=0$ at relatively short times. Note that, especially for small islands, there are still considerable excursions in the values, which can be associated with the addition of individual pixels. In these calculations, rectangular (mm) symmetry is preserved, so that four pixels are added at once; clearly the excursions might be smaller if individual pixels were added. However, in that case it would be impossible to avoid introducing a statistical element, where individual pixels were added on an unknown side of the island. Including such statistical fluctuations is clearly an important next step, but the present examples are all deterministic and can serve as a point of reference.

What is noticeable in Fig. 4(a) is that the larger peaks in the capture numbers are associated with adding the first new pixels to a just completed edge. This pixel, which protrudes into a steeply rising concentration field, attracts a far greater flux than a smooth face. This effect, which is a well known cause of roughening and dendritic branching, occurs in this model at the single adparticle level.[23] Moreover, since the entire diffusion field is coupled, adparticles attached to the x side, for example, can strongly suppress subsequent capture by the y side (or vice versa), even though no-corner rounding is allowed. Thus σ_x and σ_y are anticorrelated, with quite large excursions, whereas the average capture number follows a smoother curve.

We can use these pixel calculations to follow the evolution of the aspect ratio of the island shape $A=(L_y/L_x)$ as the island grows with no corner rounding, as shown in Fig. 4(a) for the (5×11) island and in Fig. 4(b) for a range of initial island shapes. Here we compare $(5\times N)$ with $(N\times5)$ islands, where $N=7$, 11, and 15, keeping $D_y=10$ and $D_x=5$ as before. The curves follow nonintegral values of L_y and L_x, by allowing suitably for the addition of individual pixels.

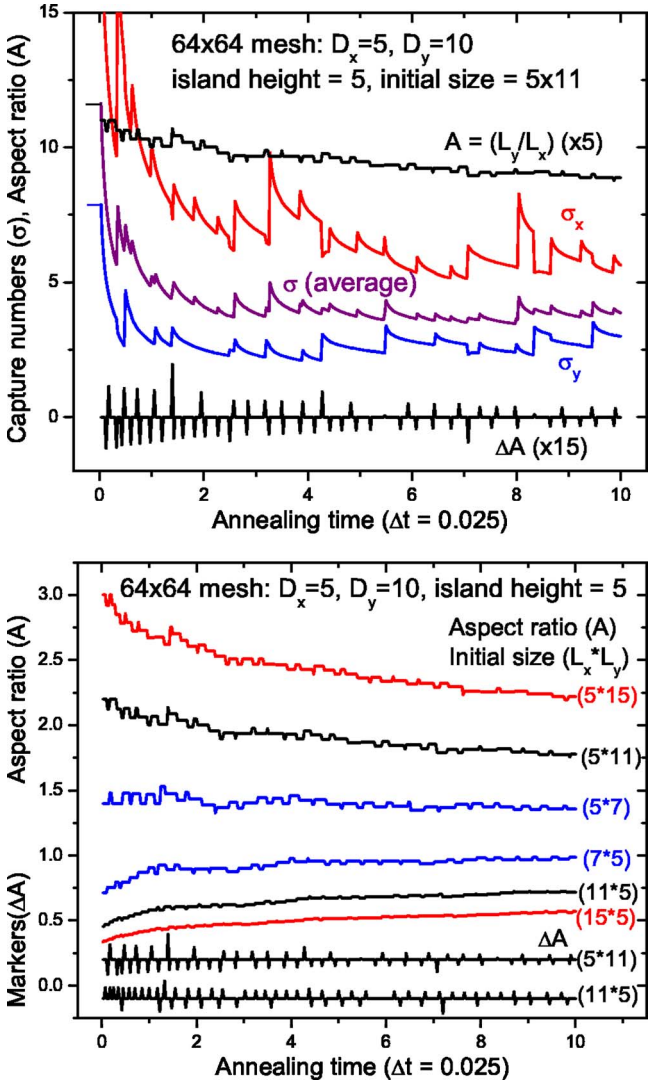

FIG. 4. (Color online) Pixel by pixel capture numbers (σ) and island aspect ratios ($A=L_y/L_x$) during early time annealing with no potential. FFT calculations with fine time steps $\Delta t=0.025$. The markers $\Delta A=A(t)-A(t-\Delta t)$ shows each individual event when L_y or L_x changes. (a) Capture numbers σ_x (upper lines, red online) and σ_y (lower lines, blue online) and the weighted average σ_y (middle lines, purple online), plus A and ΔA (black lines) for an initial 5×11 island. (b) Comparison of aspect ratios A for initial island sizes ranging from 5×15 to 15×5 (color online) with ΔA (black lines) for 5×11 and 11×5 islands. See text and Table I for discussion.

As annealing proceeds, all these islands become squarer, but at different rates; the fastest rate of approach occurs when the longer side is fed by faster diffusion. This result can be discerned from the comparison, shown in Table I, of A for the $(5\times N)$ islands with A^{-1} for the $(N\times5)$ islands; initially these are the same, but A^{-1} values, i.e., (L_x/L_y) drops further, and at a greater initial rate. There are many interesting pixel-level details that can be gleaned from Fig. 4(b), Table I, and from curves of σ_x and σ_y for all these cases. The difference $\Delta A=A(t)-A(t-\Delta t)$ shows each individual event, when L_y or L_x changes; positive spikes correspond to in-

TABLE I. Capture numbers (σ) and aspect ratios (A) for islands of different shapes. [See Fig. 4 for overview. The values given are approximate, as read off graphs similar to Fig. 4(a); to quote higher accuracy from the plotted data would be spurious, as the exact value would then depend on exact times t and the value of Δt.]

Initial size	$\sigma_x(t=0,10)$	$\sigma_y(t=0,10)$	$A(t=0,10)$	A^{-1} at $(t=0,10)$
5×15	26, 6	8, 3	3.0, 2.25	
5×11	19, 6	8, 3	2.2, 1.8	
5×7	12, 4.5	8, 3	1.4, 1.35	
7×5	8.5, 4.0	11, 3.3	0.71, 0.95	1.4, 1.05
11×5	8.5, 4.0	17.5, 4.0	0.45, 0.70	2.2, 1.40
15×5	8.5, 4.5	24, 4.5	0.33, 0.55	3.0, 1.75

creasing L_y and negative spikes to increasing L_x. Thus, for example, as shown at the foot of Fig. 4(b) the pattern of $\Delta A(t)$ (the event markers) is completely different for the (5×11) and (11×5) islands.

Although these examples shown here are completely deterministic, the individual σ_x and σ_y and A curves shown in Fig. 4 can resemble statistical behavior over the long term. Individual excursions are completely reproducible, although they should probably not be over-interpreted. In particular, for very short time steps, the sharp onsets of the changes described here can represent less than one adparticle being added to the island. This may be a good reason, in addition to speed of execution, for settling on a relatively modest time resolution, as further detail results in "empty magnification."

The other limit is no corner barrier, or *free corner rounding*, which should make the island grow uniformly on x and y edges, such that the initial edge-length difference is preserved. In a continuum model, it is "obvious" that the adparticles can diffuse anywhere around the island periphery, and that "therefore" the difference (L_y-L_x) remains constant. But if we are interested in exploring atomic level processes, this case will never arise, and the details of edge nucleation need to be considered. For example, if adparticle edge diffusion were so rapid that nucleation could occur anywhere around the island perimeter, then all symmetry has been lost from that moment onwards. Adding a repulsive potential may even decrease the interest of the results somewhat. First, the growth is much less than without the potential; second, the island shape that results is dominated by the shape of the potential, which can of course be different on each edge. We consider that deterministic-statistical hybrid models of this type, with edge nucleation and other types of fluctuations, may be interesting avenues to explore in future work.

V. DIFFUSION, DIRECT IMPINGEMENT, AND NUCLEATION DURING DEPOSITION

A. Nucleation densities relevant to nanofabrication

Extra terms can be simply added in real space into the MED equations to deal with deposition and with direct impingement, as is common in rate equation treatments. New nuclei can be added at times determined statistically.[24] As noted previously,[7] repulsive fields around islands slow down diffusive capture, and thereby make direct impingement a more important contribution to growth of the islands. When the repulsive potential is zero, it is well known that the low coverage nucleation pattern when all islands are stable ($i=1$) is determined by the parameter (D_1/F); experimental values lie in the range $10^3<(D_1/F)<10^9$ (see, e.g., Refs. 2, 8, 12, and 13 particularly). For short simulation times, we need to use relatively small values of (D_1/F) towards the lower end of this experimental range, or else find a realistic way to increase the allowable time steps. The hybrid-FFT method is a means of extending the real time scale, as at longer times there are fewer important Fourier spatial frequencies, as described in Appendix D.

TABLE II. Domain sizes and corresponding nucleation densities. [Last column is for the atomic density of Si(001), 6.78×10^{14} cm^{-2}.]

Domain Size ($N\times M$)	Nucleation density (ML)	Nucleation density (cm^{-2})
16×16	3.91×10^{-3}	2.65×10^{12}
32×32	9.77×10^{-4}	6.62×10^{11}
64×64	2.44×10^{-4}	1.66×10^{11}
128×128	6.10×10^{-5}	4.14×10^{10}
256×256	1.53×10^{-5}	1.03×10^{10}

As we become more interested in true nanofabrication and self-assembly in the nanometer scale range, these lower values are more and more realistic. As Table II shows, one island at the center of an $N\times M$ mesh of points corresponds to a nucleation density, $n_x=(NM)^{-1}$ in ML units, if each mesh point corresponds to a single adparticle or atom. Since for $i=1$, the maximum density $n_x=0.25(F/D_1)^{1/3}$, we can see that we need to have a 64×64 mesh to simulate the maximum density for $(D_1/F)=10^9$, and $(D_1/F)=10^6$ could already be simulated realistically with less than 16×16 mesh at atomic resolution. Of course it is also known that accurate computation using continuum equations typically requires a few (linear) mesh points per adparticle;[25] but if we are primarily interested in rapid visualization with moderate accuracy, then smaller meshes will suffice. For example, if we settle on 64×64 mesh as in Figs. 1–4, then we could visualize the growth of a single island at a density of 2.44×10^{-4} ML, and then introduce a ten-fold increase in island density via (statistical) nucleation before reaching the maximum density for $(D_1/F)=10^6$, 2.5×10^{-3}ML.

With the repulsive potential, the maximum density is higher, so the nucleation pattern can be followed even further; however, computing time increases linearly with (D_1/F), since the time step $(D_1\Delta t)$ has to remain small, and if F is too small, not much changes in a time step. But it should be emphasized that we are not introducing all the parameters at once, so here we say nothing about nucleation *per se*, which depends on a lateral binding energy E_b that is not in the problem as studied here. For example, if $i>1$, due to finite (E_b/kT), then n_x is smaller than the above $i=1$ case,[1,2] and so there is no inconsistency in studying the

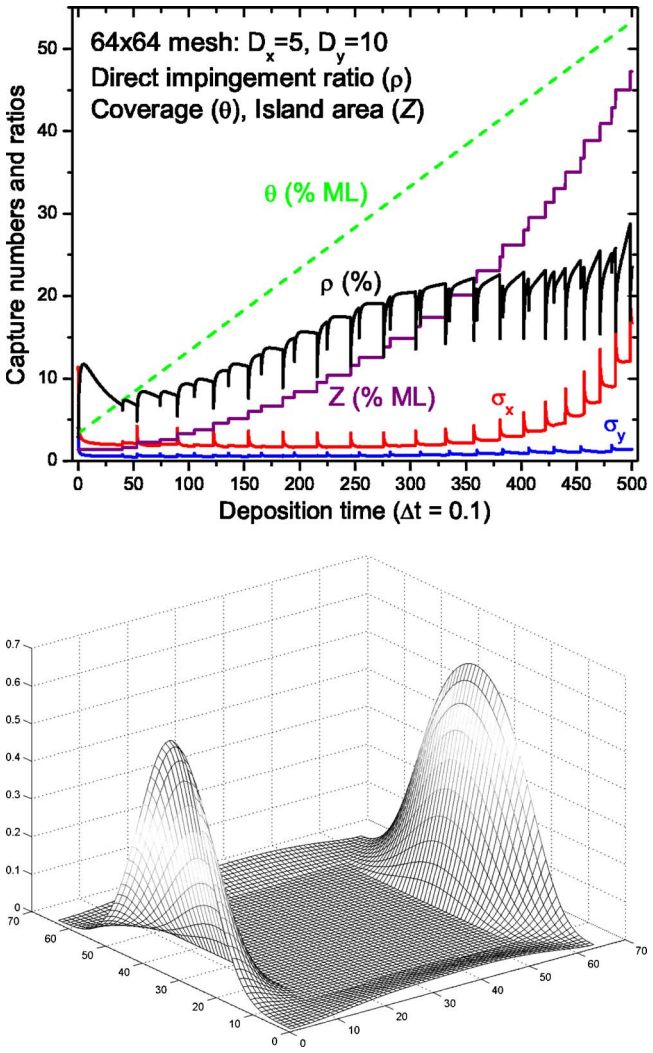

FIG. 5. (Color online) (a) Ratios as indicated and capture numbers during deposition for a rectangular potential with initial maximum $\beta V_m = 1.87$ at the edge of the 5×11 island. The direct impingement ratio ρ (black line), total coverage θ (dashed line, green online), and relative island area Z (stepped curve, purple online) are plotted as a function of deposition time, with values of capture numbers σ_x (upper line, red online) and σ_y (lowest line, blue online). (b) Contour plot of field concentration at $t=500$, showing the island with $Z \sim 0.45$ ML, and high field regions between islands along the x axis. See text for discussion.

growth of a single island at lower than the maximum density. This has the additional advantage that the field concentration $c(\boldsymbol{r})$ is higher than in the $(i=1)$ case, and the growth rate is faster with other parameters constant.

B. Deposition and direct impingement

The equation to be solved on the grid is the analog of the MED Eq. (9) with additional flux terms for the field c_i, and corresponding direct impingement terms for the island

$$\partial c_i/\partial t = \sum_j [W_{j\to i} c_j - W_{i\to j} c_i] + F, \qquad (12)$$

where it is understood that the flux F is masked onto the field or the island as appropriate. The island mask in this example is also split as in previous examples, to apportion the flux to the x and y edges. Thus we are not concerned here with second layer growth, Ehrlich-Shwoebel barriers, or any such well-known elaborations; the particles are added to the nearest edge of the 2D island.

For Fig. 5, we solved Eq. (12) with a small constant initial field concentration, starting from a 1 ML height 5×11 island with the weaker potential of the two shown in Fig. 2, and investigated the relative importance of direct impingement to diffusion capture. Direct impingement can often be neglected in the early stages of growth,[1,2] since it contributes in proportion to the relative island area Z, whereas the field contribution is proportional to $(1-Z)$. But it has been included in recent papers on nucleation and growth,[7,13] because it must become more important at higher coverage θ.

In Fig. 5(a) $(D_y/F) = 10^4$, deposition starts at time zero onto a substrate containing the island and a uniform concentration field $c = 0.02$ ML. We plot the direct impingement ratio ρ, which is just the ratio of growth increments from direct impingement and diffusion capture in each time step; the island size is incremented line by line [see Fig. 9(b)], so this leads to the steps in Z, which serve as event markers; the total coverage θ, however, increases linearly. The capture numbers σ_x and σ_y are also shown; both stay low for much of the deposition time shown, as the potential becomes more strongly repulsive as the island size increases. The upward going spikes in the capture numbers correspond to incrementing the island size, and these spikes are mirrored in the ratio ρ, since diffusion capture is the denominator of this ratio. The value of ρ rises fairly linearly to ~ 0.2, when $\theta \sim 0.25$ ML, but then levels off, not reaching much more than 0.25 at $\theta \sim 0.5$ ML; over the same time range, σ_x starts to rise sharply, while σ_y stays low, and even decreases.

This behavior is against our expectations but the reason is not hard to discern from other (2D) figures produced at the same time; one of these is shown in Fig. 5(b). The concentration along the y direction is strongly suppressed by two factors, the larger value of $D_y = 2D_x$, and the close overlap between the potential fields along this direction; this yields a diffusion current towards the pockets between islands in the x direction. The concentration field builds up here strongly, to very high levels, ~ 0.6 ML in the case illustrated in Fig. 5(b) for a total deposit of ~ 0.45 ML.

Because nucleation is excluded in the present numerical examples, only capture by diffusion in the x direction can limit the concentration. Of course, if nucleation were included, these are exactly the locations where subsequent islands would (statistically) form and then grow, as seen in Ref. 24. Note, however, that the island shape of Fig. 5 is much squarer than the initial island shape: the 5×11 island becomes 29×37 at $t=400$ and 43×47 at $t=500$. Thus the approximate aspect ratio decreases from 2.2 through 1.28 at $t=400$ to 1.15 at $t=500$. This is primarily because the potential strength used increases substantially as the island size increases.

C. Anisotropic repulsive potentials and the growth of nanowires

The growth of nanowires is of considerable current interest.[26–28] Thus we are interested in the conditions under

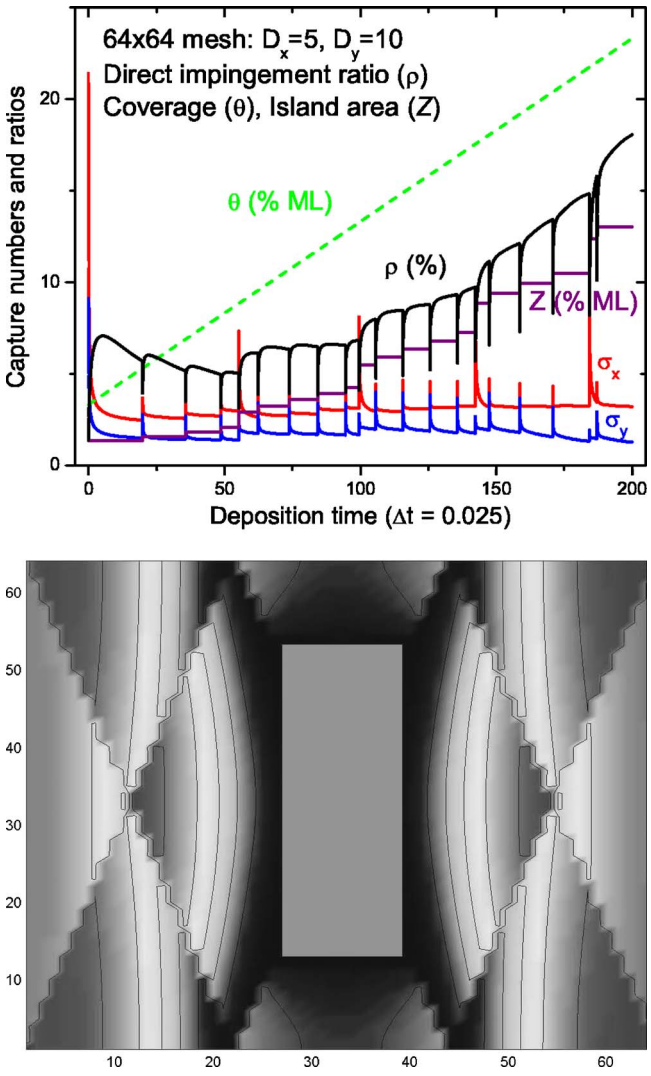

FIG. 6. (Color online) (a) Ratios as indicated and capture numbers during deposition for a highly anisotropic rectangular potential V_x, with only the x side included at the edge of the 5×11 island ($V_y=0$). Otherwise all quantities calculated are as Fig. 5(a), but with finer time steps $\Delta t=0.025$. (b) Plan-view plot of field concentration at $t=200$, showing the elongated rectangular island with $Z\sim0.18$ ML, and high field channeled regions between islands along the y axis, which are modified by repulsive fields from neighboring islands (diagonal edges in the contours). The island gray level has been lightened for clarity; see text for discussion.

which these wires may grow. It is clear from the current study that diffusion by itself goes in the opposite direction, even with no corner rounding, via the coupled diffusion fields around the x and y sides, as shown during annealing in Fig. 4; a strong potential surrounding all sides also does not produce wires in deposition, as demonstrated in Fig. 5. We can, however, show using Fig. 6 that a very anisotropic potential can produce wires, or at least a strongly increasing rather than decreasing aspect ratio. For this test, we note that the repulsive potential we are using consists of separate portions for the x and y sides; here, we simply remove the potential on one of these sides. For the 5×11 island, the most favorable strategy is to keep the potential hindering attachment to the longer side that leads to σ_x, and remove the potential responsible for the short side σ_y.

As illustrated in Fig. 6(a) up to $t=200$, there are now many more "spikes" in σ_y, even though the absolute value is still much smaller than σ_x. We can count these spikes to track the changes in island size and shape, noting that the 5×11 island becomes 9×25 by $t=100$ and 13×41 by $t=200$, with approximate aspect ratios of 2.2, 2.78, and 3.15. However, even in this extremely anisotropic case, with an increasingly repulsive potential V_x, growth is not completely suppressed on the longer side, as the concentration remains high there, yielding a relatively high value of σ_x. This concentration distribution can be seen in the plan view concentration field contours shown in Fig. 6(b), where the island size and shape is such that neighboring islands strongly influence the concentration; fast diffusion ($D_y=2D_x$) to the short (σ_y) sides drain the field efficiently, but the repulsive V_x fields from the neighbors cut off the supply, and almost all the remaining field concentration is in lines along the y axis between the "wires." As deposition continues, σ_y decreases, and the complex overlapping diagonal patterns in Fig. 6(b) grow in relative strength, due to the relatively strong long range potential used.[29] Similar concentration fields, without the diagonal patterns, are observed for short range, barrierlike, potentials which are calculated to be realistic for monolayer height Ge islands on Si(001), as described in the following section.

VI. DISCUSSION: CASE STUDIES WITH Ge/Si(001) PARAMETERS

Since the methods described in the present work are quite general, we have not so far discussed the specific values needed for comparison with any one material system. As a case study, we now consider potentials which are calculated to be reasonably realistic for Ge/Si(001). It is well known from other work[30–32] that the potential in the Ge/Si(001) case is steeper than that of Fig. 2(a), and is almost similar to a δ function edge barrier. The barrier height is thought to be in the range 0.35–0.55 eV for Ge on Ge/Si(001); the diffusion energy E_d can also vary with strain.[33,34] These absolute values mean that we need to discuss temperature in order to obtain the value of βV_m, corresponding to the maxima around the island edge. For example, if $T=450$ °C (723 K), and $V_m=0.35$ eV, then βV_m is ~5.6, so that we can expect a large reduction in capture numbers during annealing at this temperature, as shown here by Figs. 2 and 3.

This feature is readily demonstrated using the techniques described in this paper for any chosen potential, and realistic potentials have been developed for monolayer height Ge islands on Si(001). A range of cases have been considered where the repulsive potential is caused by strain energy, based on force monopoles at the edge of the islands within anisotropic elasticity.[35] This work yields explicit expressions for ε_{xx}, ε_{xy}, and ε_{yy} for rectangular islands, and hence the potential, which scales as ε^2; this potential has realistic maximum values $V_m\sim0.3$–0.4 eV; as evaluated here for 450 °C, $\beta V_m\sim3$ initially and increases to a maximum ~6 as the islands grow.

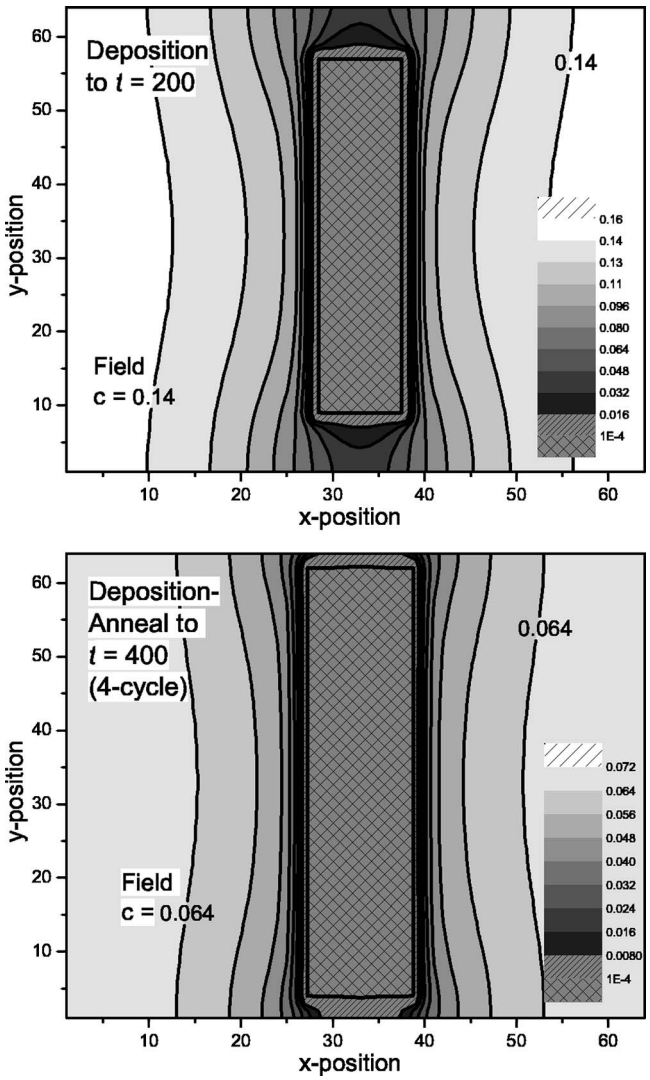

FIG. 7. Contour plots of wire growth with anisotropic Ge/Si ML potential with strain components $\varepsilon_{x0}=0.04$, $\varepsilon_{y0}=0$, the cross-hatched region representing the island, which had initial size 5×11. The other parameters $D_y=2D_x=10$ and $(D_y/F)=10^4$ are the same as in previous figures. (a) Continuous deposition to $t=200$, such that the diffusion distance is 77.5; the contours are at concentration intervals $\Delta c=0.016$ ML. (b) Deposition plus annealing in four-time cycles of 100 to $t=400$, with contours at $\Delta c=0.008$ ML. The diffusion distance is therefore ~110 overall and ~55 in each deposition or anneal period. Other data for the same conditions are in Table III cases (a) and (c); see this table for other cases and the text for discussion.

The symmetric case for Ge/Si(001) has mismatch strain $\varepsilon_{x0}=\varepsilon_{y0}\sim0.04$, but one can also investigate cases appropriate in general to many silicide wires, where the potential is anisotropic, by relaxing the strain in one dimension. The case where $\varepsilon_{x0}=0.04$, $\varepsilon_{y0}=0$ is illustrated here, one of six cases presented elsewhere.[35] The other parameters $D_y=2D_x=10$ and $(D_y/F)=10^4$, are kept the same as for previous figures, notably Fig. 6(b). In Fig. 7(a), we illustrate this case, and see that wirelike geometry results after deposition to $t=200$. The effect is stronger than in Fig. 6(b) because, although the potential does increase somewhat if the x width increases, the potential does not vary much with the y length of the wire. Thus the pinch-off effects seen in Fig. 7(a) are much less marked, and the following calculations were done without the "ring of eight" potentials; see Fig. 8(a) in Appendix B for clarification.

The combined effects of deposition and annealing can also be studied with any potential on any size mesh, and these variables can be used to explore the effects of nucleation density and the disposition of neighboring crystals. Here we show that alternate periods of deposition and annealing can lead to more pronounced wirelike shapes, as shown in Fig. 7(b) and Table III. Figure 7(b) shows the effect of a four-cycle deposition-anneal sequence to $t=400$, while Table III follows the shapes of the island for several different deposit-anneal sequences to $t=400$ (the same total dose as Fig. 6), and varying the mesh size and shape. Two different initial island sizes are considered in this table, the 5×11 as illustrated in Fig. 7, and the ultranarrow 1×3 starting size, which results in the most wirelike aspect ratios (>8). This last case is at the limit of applicability of the MED method, since the initial island width is the same as the grid size.

These phenomena can be understood by the following considerations. During deposition, the concentration builds up in pockets parallel to the wire axis, as shown in Fig. 7(b), to the point that diffusive capture by the long sides is possible, even though the "easy" path is diffusion to the short (nonstrained) sides; this causes modest growth in the x direction, in part due to direct impingement. However, during the annealing period, this high concentration in the pockets drains away to the short side, causing further diffusive capture in the y direction and no growth in the x direction, since there is no direct impingement contribution. On resuming deposition, the pockets are re-established, but by a suitable choice of on/off ratio (the two-, four-, and eight-cycle anneals given in Table III, or any other anneal sequence), the field maxima may be controlled, and growth in the y direction may be manipulated. Note that these deposit-anneal sequences can also produce "better" wires than simply depositing at half the flux, although the effects of the neighbors are stronger in the cases studied so far.

The effects of the neighboring crystals can also be seen via Table III. For the deposit-anneal sequences shown, the aspect ratio of the wires saturates and then slowly reduces once the wire length approaches the mesh size, as the neighboring wires approach each other, and σ_y declines. If the neighbors are arranged on a narrow mesh with the same area, where wire growth is parallel to the long axis of the mesh, growth starts out the same, but continues unimpeded by the neighbors, faster and for longer; the low value of the final field maximum is actually in a band perpendicular to the wires, because of the different mesh shape. Similar effects can be obtained by working at twice the area (half the nucleation density), where for longer times there is a larger number of adparticles to drain from the field, also resulting in longer wires with comparable width. There are many more cases that could be studied with this program and parameters; but these results already show that interrupted deposition, on a suitably shaped array of nucleation centers, may be an interesting approach to creating nanowires, provided that the temperature is low enough that the island shape cannot

TABLE III. Deposition and annealing: Wire sizes, aspect ratios, and field maxima for ML islands with Ge/Si parameters. All table entries are in the order: integral island size, aspect ratio (bold), and maximum field concentration; the upper and lower rows are for initial (1×3) and (5×11) islands, respectively. Aspect ratios result from including the display pixels, as in Fig. 9(c); the integral size is incremented as in Fig. 9(b). Conditions: 64×64 mesh; (a) deposition to $t=200$, then anneal to 400; (b) deposition to $t=100$, anneal 200, and then repeat; (c) deposition to $t=50$, anneal to 100, repeat three more times; (d) all deposition but half the flux; (e) as (b), but 32×128 mesh; (f) as (b) but 64×128 mesh. All other conditions as in Fig. 7, see text for discussion.

Initial size $(1\times3/5\times11)$	$t=100$	$t=200$	$t=300$	$t=400$
(a) 2-cycle	3×27, **7.13**, 0.109	7×55, **7.23**, 0.158	9×61, **6.02**, 0.095	11×63, **5.53**, 0.061[b]
anneal[a]	5×25, **4.03**, 0.106	9×49, **5.08**, 0.153	11×59, **4.91**, 0.087	13×61, **4.64**, 0.052
(b) 4-cycle	3×27, **7.13**, 0.109	5×45, **7.66**, 0.070	7×59, **6.82**, 0.127	9×61, **5.89**, 0.079
anneal	5×25, **4.03**, 0.106	7×41, **5.02**, 0.065	9×53, **5.05**, 0.122	11×59, **4.77**, 0.071
(c) 8-cycle	3×23, **7.13**, 0.060	5×41, **7.55**, 0.079	7×55, **7.17**, 0.084	9×61, **6.07**, 0.090
anneal	5×23, **3.72**, 0.057	7×37, **4.83**, 0.075	9×51, **5.14**, 0.080	11×59, **4.84**, 0.083
(d) deposit,	1×21, **7.70**, 0.064	5×39, **7.45**, 0.087	7×53, **7.26**, 0.095	9×61, **6.27**, 0.101
flux/2	5×19, **3.40**, 0.061	7×35, **4.61**, 0.084	9×49, **5.09**, 0.091	11×57, **4.90**, 0.095
(e) narrow mesh,	3×27, **7.17**, 0.115	5×47, **8.24**, 0.078	7×69, **8.47**, 0.119	9×83, **8.77**, 0.034[c]
4-cycle	5×25, **4.03**, 0.111	7×43, **5.37**, 0.073	9×61, **6.01**, 0.116	11×75, **6.52**, 0.037[c]
(f) twice area,	3×27, **7.17**, 0.118	5×51, **8.17**, 0.098	9×79, **8.17**, 0.162	11×99, **8.23**, 0.104
4-cycle	5×27, **4.12**, 0.116	7×47, **5.54**, 0.095	11×71, **6.05**, 0.159	13×91, **6.43**, 0.100

[a]Deposition only values correspond to the first two columns of the two-cycle anneal.
[b]The wire spans the mesh and does not quite reach $t=400$ before coalescing into an infinite wire, due to the periodic boundary.
[c]The low value of the maximum in this case corresponds to a different location in the mesh, in a band perpendicular to the wire direction.

equilibrate via corner rounding edge diffusion.

For further detailed results specific to the Ge/Si system, one may need to model in addition the marked diffusion anisotropy, whose principal axes are at 45° to the edges of the hut clusters, taking account the fluctuating state of the wetting layer, and incorporate for example, the physical mechanism of the hut to dome transition.[36] We can attempt to model such effects on the island (on average) by resetting the concentration at the end of each time step to the equilibrium adparticle concentration at that temperature, rather than to zero as done here. We can apply 2D nucleation models based on the concentrations that are present, both during deposition and annealing, and subsequently follow the time dependence in the presence of new nuclei. It is clear that such work has to concentrate on one of these features at a time, not all at once, as the time scales involved vary over a huge range.

VII. CONCLUSIONS

In conclusion, we have set out the differential equations needed to solve for time-dependent capture numbers and other growth quantities in the presence of general (two-dimensional) potential fields. The analytic theory is described in Sec. II and Appendix A. Numerical methods and experimentally relevant examples are given in the remainder of the paper. An FFT method, published previously,[9] has been shown to be efficient in the case of zero potential, as detailed in Appendix B. The main body of the paper is based on the recent master equation discretization (MED) algorithm,[11] which incorporates the underlying dynamics exactly as explained in Sec. III. An accurate hybrid-FFT scheme is also introduced which may have speed advantages for small potential fields and long times, as discussed in Appendixes B and C.

The results obtained with the MED and hybrid-FFT schemes have been demonstrated in rectangular geometry. These schemes have been used to illustrate the reduced capture numbers obtained when there are repulsive potentials between adparticles and clusters. The case of "no corner rounding" has been explored in detail, where quantitative capture numbers, island aspect and direct impingement ratios have been obtained, during annealing in Sec. IV and during deposition in Sec. V. All results can be produced as movies, where one frame is produced at most every Δt. Some of the time constraints are discussed in Appendix D. The present methods are fast: for example the data for Figs. 5 and 6 were produced by two separate single calculations taking about 70 s each. This contrasts with several competing methods described elsewhere,[8] which typically require long times on supercomputers or large PC clusters.

For physical systems, we have concentrated on Ge/Si(001) and metal silicides, and shown that these MED methods are applicable, as detailed in Sec. VI. We have demonstrated in Secs. IV B and V B that calculations approximating to Ge/Si hut clusters, where the adparticle-cluster repulsive interaction increases initially with particle size,

leads to a growth slow-down that is substantial at moderate to low growth temperatures ~400–500 °C, in line with many experimental observations.[35] In these conditions, diffusive capture over the repulsive barrier is reduced, and direct impingement is an important component of the growth flux. During annealing, such structures are highly metastable over long times as is experimentally observed. We briefly discuss nucleation and growth on facets on hut clusters in terms of a 2D nucleation and growth mechanism.[36]

The second material system considered consists of a range of silicide nanowires. What we have shown here in Secs. V C and VI is that strongly anisotropic repulsive potential fields can be one factor contributing to wire growth. We also emphasized that interrupted deposition can be effective in promoting wire growth. However, the details certainly depend on the magnitude and form of the potential, and the relative disposition of neighboring islands. There are of course other possibilities for creating strongly anisotropic wires, that are not directly due to repulsive fields *per se*, but due to anisotropic attachment, and including growth into, rather than on, the substrate.[26] In that case, we cannot consider the island and the island edge to be a perfect sink as we have done here, but must consider partial sinks at the edge of the island, and diffusion over, and imperfect incorporation into the island.[37] For a full 2D or 3D exploration of such effects, we may well have to include all such effects: anisotropic potentials and attachment, diffusion over the islands, and partial sinks, plus strongly nonlinear effects such as nucleation.

All the work described here uses deterministic partial differential equations applied to linear-scaling situations. There is potential for using the same basic continuum approach, coupled with statistical interactions and fluctuations,[24] to problems in which nucleation, growth and annealing are combined in ways that illustrate real experimental materials processes.

ACKNOWLEDGMENTS

The authors acknowledge important initial input from T.J. Newman and A. Sobolev. We thank R. Grima, F. Liu, and C. Ratsch for detailed advice and input from joint work, and P.A. Bennett, J. Drucker, and N. Ma for useful conversations, and permission to describe current work in outline prior to full publication.

APPENDIX A

There are no analytic solutions for the general form of Eq. (5), even in radial geometry. But, in the general case, we can expand the last two terms to obtain

$$\partial c(\boldsymbol{r})/\partial t = G - c(\boldsymbol{r})/\tau + D\nabla^2 c(\boldsymbol{r}) + \boldsymbol{A}\cdot\nabla c(\boldsymbol{r}) + \boldsymbol{B}\cdot\nabla[\beta V(\boldsymbol{r})]. \tag{A1}$$

The first four terms of Eq. (A1) are the same as those derived from Eq. (1) in the absence of a potential field. The magnitude of these two terms are controlled by gradient vector operators $\boldsymbol{A}$ and $\boldsymbol{B}$, in the scalar product form

$$\boldsymbol{A}\cdot = \{\nabla D + D^*\nabla[\beta V(r)]\}\cdot;$$

$$\boldsymbol{B}\cdot = [c(\boldsymbol{r})\nabla D^* + c(\boldsymbol{r})D^*\nabla]\cdot. \tag{A2}$$

The combination of Eqs. (A1) and (A2) represent the most general equation we wish to consider. There are several simplifications to Eq. (A1) that may be appropriate. Perhaps the most obvious is to separate out the effects of concentration on diffusion coefficients, by writing $(D/D^*)=f_t(\mathrm{c})$, where $f_t(\mathrm{c})$ is the thermodynamic factor. For low concentration, $f_t(\mathrm{c})=1$, and hence there is only one diffusion coefficient, notionally the tracer diffusion coefficient, which we write as $D^*=D_1$ to avoid confusion. However, D_1 can still be a function of position.

In the more restrictive limit that D_1 is constant, the terms ∇D and ∇D^* in Eq. (A2) will disappear, leaving the extra terms in Eq. (A1) of the form

$$\boldsymbol{A}\cdot\nabla c(\boldsymbol{r}) + \boldsymbol{B}\cdot\nabla[\beta V(\boldsymbol{r})] = D^*\nabla[\beta V(\boldsymbol{r})]\cdot\nabla c(\boldsymbol{r}) + \{c(\boldsymbol{r})D^*\nabla^2[\beta V(\boldsymbol{r})]\}; \tag{A3a}$$

this equation can be rearranged as

$$\boldsymbol{A}\cdot\nabla c(\boldsymbol{r}) + \boldsymbol{B}\cdot\nabla[\beta V(\boldsymbol{r})] = D_1\nabla\{c(\boldsymbol{r})\cdot\nabla[\beta V(\boldsymbol{r})]\}, \tag{A3b}$$

as in Eq. (6). If $D^*\neq D$ the remaining terms, the difference between the last two terms of Eq. (A2) and those in Eq. (A3), are cross-terms involving the gradients of the diffusion coefficients, namely,

$$C = \nabla D\cdot\nabla c(\boldsymbol{r}) + c(\boldsymbol{r})\nabla D^*\cdot\nabla[\beta V(\boldsymbol{r})]. \tag{A4}$$

We can see that C may well be small, based on the following argument. If the potential effects are large, then $c(\boldsymbol{r})$ will be dominated by equilibrium effects, such that $c(\boldsymbol{r})\cong c_0\exp[-\beta V(\boldsymbol{r})]$, where c_0 is a constant. Thus $\nabla c(\boldsymbol{r})\cong -c(\boldsymbol{r})\nabla[\beta V(\boldsymbol{r})]$, and Eq. (A4) can be written

$$C \cong -c(\boldsymbol{r})(\nabla D - \nabla D^*)\cdot\nabla[\beta V(\boldsymbol{r})]. \tag{A5}$$

Thus C vanishes at low concentration, where $D^*=D$, and corresponds approximately to an extra contribution to the loss term $-c(\boldsymbol{r})/\tau$ in Eq. (5) in the general case. This means that we do not need to consider equation (A5) separately, and we will neglect it in this paper.

APPENDIX B

The numerical methods used in this work have been published in some detail in a previous conference paper.[9] The topics discussed there include a demonstration of the FFT method of solving the time-dependent diffusion, by checking against the known solution for an array of point sources on a lattice. The sources consisted of a central point source, surrounded by one or more rings of extra sources, which ensure periodic boundary conditions; the first "ring" contains eight extra sources, as shown in Fig. 8(a). These sources were needed once the diffusion field from the central mesh of points spreads into neighboring areas. The FFT method itself

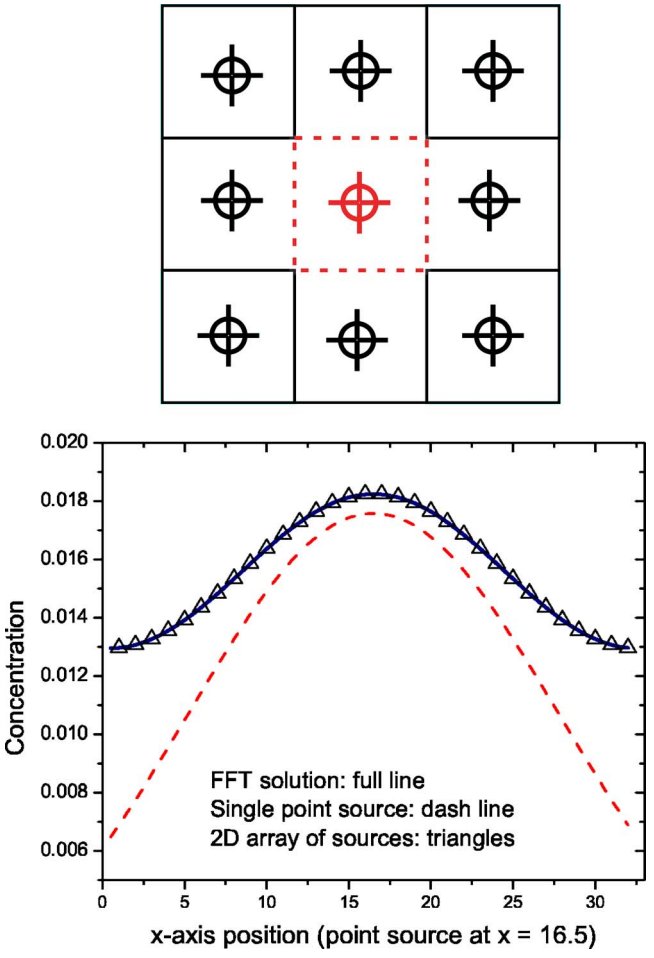

FIG. 8. (Color online) (a) Schematic diagram of a 2D array of point sources, consisting of a central source and a ring of nearest neighbors. (b) Comparison of the FFT central x-axis solution (full line, blue online) with single point source (dash line, red online), and 2D array (black triangles), after annealing for $t=6.4$ with $D_x=5$, $D_y=10$, on a 64×64 grid with grid size $a=0.5$ (after Ref. 9). See text for discussion.

is a 2D pbc solution, and so needs to be compared with the 2D-analytic solution for a source array, as in Fig. 8(b). We showed that this FFT method could be expressed very concisely in MATLAB®6.5 and was essentially exact except at very short times, when discontinuities in concentration are present.[9]

In the present work, we use the same "ring of 8" approach to make sure that the potential function corresponds adequately to periodic boundary conditions. In addition to the central function, which is all that is needed for small islands near the center of the mesh, the tails of the surrounding (8) potential functions are added once the potential starts to overlap into the surrounding mesh, i.e., when the potential fields from neighboring islands overlap. This ensures that the adparticle concentration has a zero gradient on the boundary of the mesh; failure of this condition means that not enough potential functions have been included.

The second numerical method[9] is the use of logical masks to delineate the island, field, and island edge regions (matrices B1, B2, and B3) on the mesh, and matrices B4 and various sub-matrices on the island. Growth of the island is effected by allowing diffusion to occur during each time step Δt, such that an adparticle concentration builds up in this time over the matrix B4. The total integrated concentration then corresponds to the growth increment (grinc), and capture numbers can be deduced directly from this value and the area and height of the island. After Δt the island concentration is reset to zero, and these adparticles are added to the island.

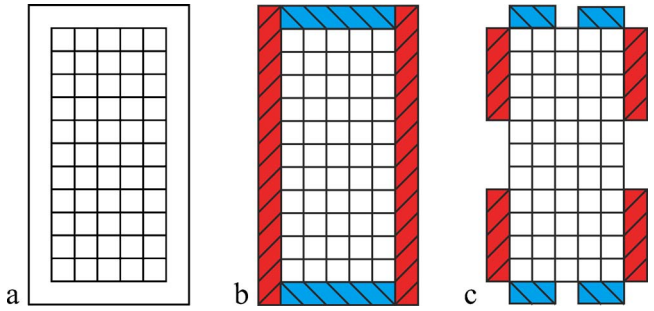

FIG. 9. (Color online) Updating island size and shape. In the examples shown here, a 5×11 island (a) grows by adding ad particles to the surrounding ring. The calculation is incremented line by line (b), first by incrementing the length in the y direction (dark shading, blue online) and then the x direction (light shading, red online). In most examples, the display is incremented pixel by pixel, as in (c) (after Ref. 9). See text for discussion.

For the case we consider in detail, restricted corner diffusion, we also use submatrices of B4, B4x, B4y, and an edge matrix B4e, to apportion the growth increment to the x and y edges, (grincx and grincy) and hence to calculate capture numbers σ_x and σ_y for each edge; these are clearly not the same for anisotropic diffusion into rectangular islands. The comparison of this case with rapid diffusion around the corners, in which only the overall growth increment is important, leads to different island shapes; any intermediate value for corner diffusion would lead to intermediate shapes, so these two extremes bracket the real situation, subject to diffusion being rapid enough along the edges in both cases.

Updating the island size and shape is a matter of counting how many particles have joined which part of the island, and then updating the size and shape accordingly. There are, of course further choices to be made at this stage, and we have concentrated on one such choice; the adparticles that join a particular edge are considered to congregate at the corners, since that is where the concentration gradient of the field is highest. One can see that such choices can branch out of control quite easily: for example, this may not be a realistic assumption with a large repulsive potential field, because the potential field may also be highest at the island corners. The point is, however, that these methods are good for introducing new processes one by one, and for making these processes explicit. A new process can be introduced and the effects explored if there is reason to expect that it may be interesting.

We have demonstrated two separate ways of updating the island size, line by line and pixel by pixel as illustrated in Fig. 9. Here we see the island size (the 5×11 matrix B4) in panel (a) being updated in panel (b) by first incrementing the

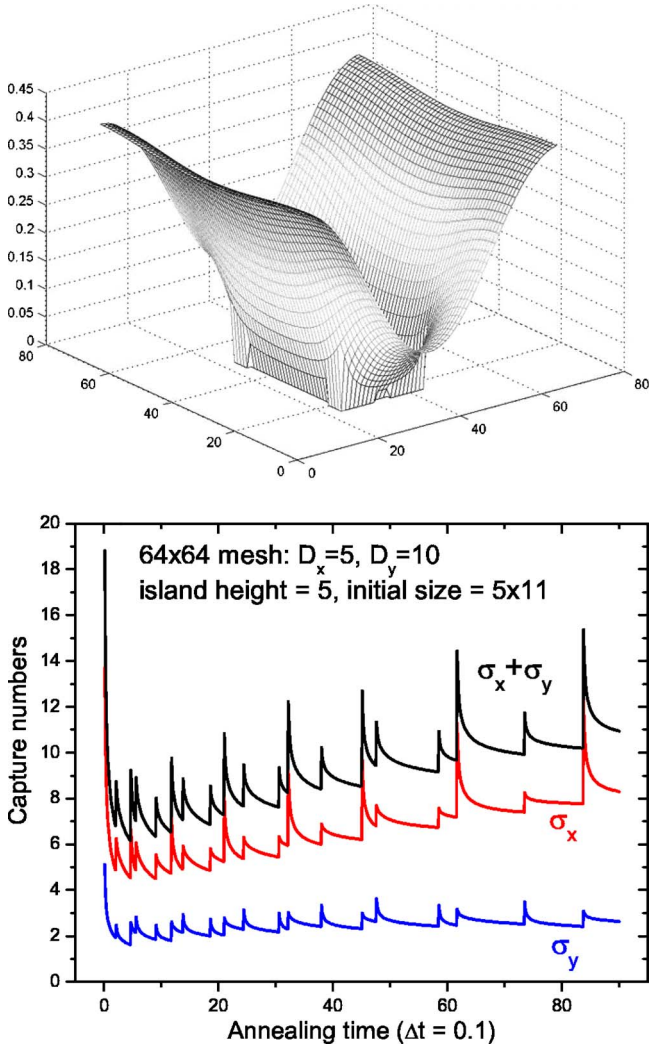

FIG. 10. (Color online) (a) Contour plots of the concentration field and (b) capture numbers for the growth of the island, after annealing for $t=90$ (900 steps, $\Delta t=0.1$) with $D_x=5$, $D_y=10$, on a 64×64 grid with step size $a=b=1$. Initial concentration=1, island height $h=5$; there is no repulsive potential in this example. The ledge growth of the island can be seen in (a) where the display is incremented as in Fig. 9(c). The jumps in the capture numbers correspond to incrementing the island size in the calculation line by line, as indicated in Fig. 9(b), as discussed in the text (Ref. 9).

y axis, and then the x axis, to produce a new B4 island of size 7×13. This updating can also be done pixel by pixel as illustrated in panel (c), but the computational cost is that *either* all the logical matrices are updated, *or* that computations are performed on the island edges, much more frequently. A compromise is to update the display pixel by pixel, to produce smooth pictures and movies as in Fig. 10(a), but to increment the diffusion field line by line. This introduces steps or "spikes" in the capture number curves shown in Fig. 10(b), and in text Figs. 1, 2, 5, and 6; these are useful for pedagogical purposes, since one can identify which spike comes from incrementing x and y edges, and interpret the rise and subsequent relaxation of the curves accordingly.

Pixel by pixel updated capture number curves are smoother, but still contain larger or smaller spikes, depending on exactly how growth is attributed to x or y edges, and how that changes when full lines are completed, and when the island corners are filled in. This method is the subject of further work; an example is shown here in Fig. 4. Depending on the time increment used, these remaining discontinuities may or may not correspond to real physics; for example, small time steps lead to sharp spikes, but the amount incremented may correspond to less than one atom added to the growing crystal. At that point, we have "empty magnification" by using a continuum description of an atomistic process.

APPENDIX C

This appendix compares three numerical methods that have been used in this work to solve Eq. (8) for the field concentration $c(\boldsymbol{r})$ in the presence of a known potential $V(\boldsymbol{r})$. We are particularly interested in accuracy, speed, and convenience within the MATLAB®6.5 environment, though many points are more general. Some points that follow were made in a conference paper,[10] but this discussion has been corrected, and is more complete, involving further numerical tests and discussions amongst the present authors.

The calculations are based on the general MED procedure published previously.[11] In the form of Eq. (9) this procedure can be readily carried out by inserting the specific values of the transition probabilities $W_{i\to j}$ from Eq. (10). Here we have generalized to anisotropic diffusion on a rectangular lattice by using diffusion coefficients D_x, D_y, and jump distances a, b as appropriate. For 2D diffusion there are eight terms in Eq. (9), four each for the x and y directions. The exponentials in Eq. (10) are readily implemented in matrix form using the MATLAB® circular shift operator, circshift($\beta V,[n_y,n_x]$), where the shift numbers $[n_y,n_x]$ are the appropriate eight combinations of $\{0,\pm1\}$.

The problem to be solved is implemented on a physical periodic domain of size $(Ma\times Nb)$. The mesh grid for the calculation can be $(M\times N)$ or integral multiples of this size, assuming that we restrict ourselves initially to uniform grids that are compatible with the student edition of MATLAB®6.5. The standard approach to integration of continuum PDEs [e.g., Eq. (8)] is to reduce the step lengths (a and b, called h in the PDE literature[11,38]) and increase the number of grid points M and N proportionately so that the physical domain size stays constant. That way, the convergence properties are checked and an optimum choice of h made. The computing time for this procedure scales with h^{-2} for the space part, and by a further h^{-2} for the time integration in simple explicit Euler schemes. Thus greater accuracy is bought at the cost of computing time that scales as h^{-4}, or equivalently $(MN)^2$.

This scaling is normally improved by using *implicit* time integration schemes. For stable implicit schemes it is desirable to keep the time step size in proportion to the mesh size, i.e., $\Delta t\sim h$, thus keeping spatial and temporal errors comparable. This results in the time scaling as Ch^{-1}. The computing time with respect to space for implicit schemes is dependent upon how efficiently we can solve a linear system of

equations of size $\sim h^{-2}$. An optimal solver will achieve computing times that scale $\sim h^{-2}$. For example, Multigrid[39] is capable of achieving this scaling, but is not considered here. This would lead to an optimal scaling for implicit schemes of Ch^{-3}, but where the multiplicative constant C could be large. Hence, implicit schemes give better stability, but this does not necessarily mean a faster algorithm for a prescribed accuracy.

At this point we have to backtrack, and address the concern that the continuum PDE solution is to be used as a means to an end, not as an end itself. The underlying problem is atomistic, provided that we are interested primarily in nanoscale islands, and we are representing island growth by finite increments of atomic rows or individual pixels as in Fig. 9. Here we are using the atomic row width as one mesh point, and this is also serving as the computational mesh for most examples. From the PDE viewpoint, increasing the size of the domain, as in Table I, results in a new problem with a different solution; since the mesh size is fixed by the atomic constraint, the scaling with h does not apply; it would only apply if the number of mesh points were further increased to improve the accuracy of the continuum solution. But this approach rapidly runs into computing time problems: it feels unsatisfactory to simulate a single adatom by say 16 mesh points, taking anything from 64 to 256 times as long, when a single point will illustrate all the points of interest in a semiquantitative manner.

The three methods used are illustrated here, using the potential of Fig. 2(a) on a 64×32 mesh, as a function of the time step Δt, with $D_x=5$ and $D_y=10$ and $a=b=1$, for an initially 5×11 island as previously. Decreasing Δt from 0.2 to 0.02 spans the range of diffusion distances in the time step ($r_d=[2(D_x+D_y)\Delta t]^{0.5}$) from 2.45 to 0.77. Figure 11(a) shows the simple five-step explicit method, namely, five integration steps during Δt, after which the boundary conditions are reapplied. The final $t=90$ corresponds to 450 time steps and 2250 integration steps for $\Delta t=0.2$ and ten times more for $\Delta t=0.02$. The former time step is too long for all but illustrative work, and the latter is around the practical limit, where we are into diminishing returns.

Similar sets of capture number plots have been obtained for the other two methods. Figure 11(b) compares the hybrid-FFT and implicit methods with the above explicit MED calculation for $\Delta t=0.05$. To be clear about the hybrid-FFT method, we give a 1D description corresponding to Eqs. (9) and (10) in which the eight terms reduce to three, such that

$$\partial c_i/\partial t = \sum [W_{i+1\to i}c_{i+1} + W_{i-1\to i}c_{i-1} - (W_{i\to i+1} + W_{i\to i-1})c_i]. \tag{C1}$$

Now we separate out terms due to the constant diffusion coefficient (D_1/a^2) to obtain

$$\partial c_i/\partial t = (D_1/a^2)[c_{i+1} + c_{i-1} - 2c_i] + \sum_j [W^*_{j\to i}c_j - W^*_{i\to j}c_i]. \tag{C2}$$

Here the first term in square brackets is just the constant diffusion coefficient equation that is efficiently solved by the FFT method, as in Appendix B. By comparing equations

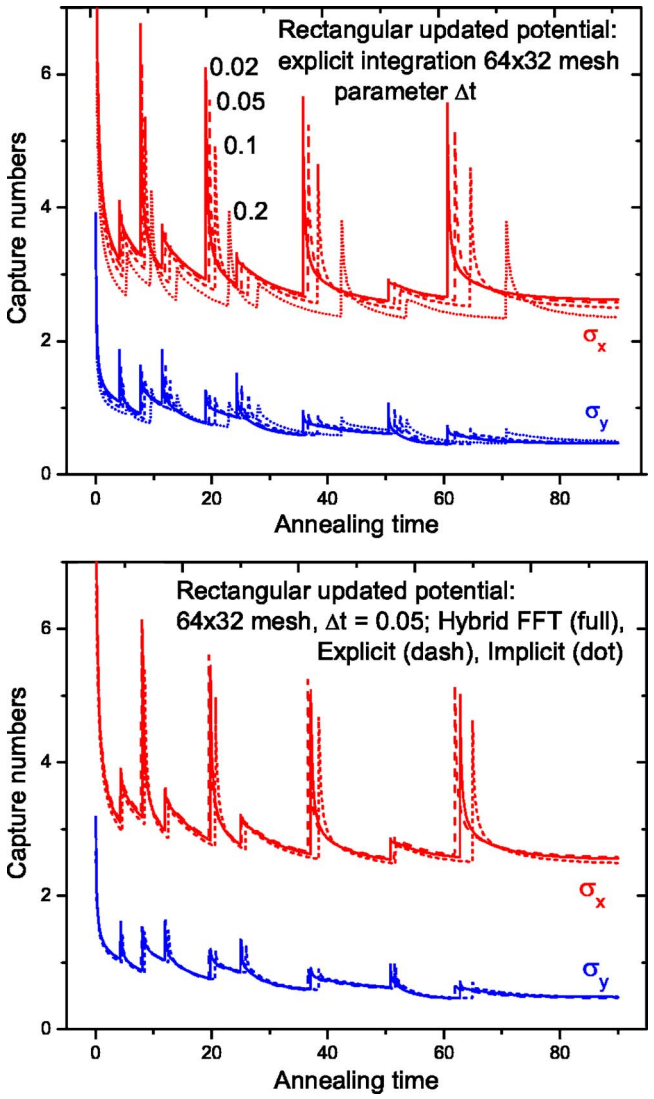

FIG. 11. (Color online) Capture numbers σ_x (upper curves, red online) and σ_y (lower curves, blue online) for the growth of the 5×11 island, after annealing for $t=90$ with $D_x=5$, $D_y=10$, on a 64×32 grid with step size $a=b=1$. Initial concentration=1, island height $h=5$, and repulsive potential as in Fig. 2(a) with the initial value of $\beta V_m=0.96$. The jumps in the capture numbers correspond to incrementing the island size in the calculation line by line, shown in Fig. 9(b); earlier, larger "spikes" correspond to more accurate solutions, which take more computing time, as discussed in the text: (a) time step Δt as parameter in the explicit integration scheme; (b) time step $\Delta t=0.05$, comparing integration methods. See text for discussion.

(C1) and (C2) with Eq. (10), we can see that the modified transition probabilities in the second square bracket $W^*_{i\to j}$ are all given by

$$W^*_{i\to j} = (D_1/a^2)\{\exp[\beta(V_i - V_j)] - 1\}; \tag{C3}$$

these terms are typically much smaller than the original transition probabilities, and vanish linearly as the potential flattens out away from the islands. In the hybrid-FFT method

these different terms (C3) were added in real space explicitly, either in four-steps or one-step per Δt.

The implicit scheme developed is a sparse matrix inversion method using a conjugate gradient scheme, constructed with MATLAB®6.5 student edition library routines (pcg and sparse). This method required extra matrix-vector-matrix conversions here; in optimized schemes, e.g., in PDELAB®, all variables are described by vectors, and so these steps are not needed. But implicit schemes do not yield any gain unless we are interested in improving scaling with h as discussed above. As seen in Fig. 11(b) for $\Delta t=0.05$, all three methods yield similar results (and even more so for $\Delta t=0.02$). The most accurate results are the five-step explicit, then the one-step hybrid-FFT (the four-step version is only very slightly better) and then the implicit method. The more accurate the method, the more the "spike" occurs at an earlier time, and the greater the maximum amplitude. But in practical terms, any of these methods is good enough for present purposes, provided Δt is small enough.

APPENDIX D

Computing times have been tabulated on a 2 GHz portable computer (Dell Inspiron 600m), and can easily be dominated by the screen printing time needed to follow the evolution of the field and capture number solutions, and by hard disk transfers. Thus large cache memory and fast graphics card are advisable for real-time (movie) presentation of such results. For no graphics in the main program loop, computing times for Fig. 11(a) with $\Delta t=0.05$ were $\sim$50 s for the one-step hybrid-FFT, and $\sim$120 s for the implicit method. Thus this procedure allows us to reduce the time step to $\Delta t=0.02$, with computing times $\sim$150 s for the hybrid-FFT, and $\sim$350 s for the implicit method. These timings are of course approximate and can be decreased by simplifying the file output further.

The explicit timings so far are a bit larger than the hybrid-FFT, and the latter method is much more stable if similar time steps are compared, for potentials that are not too strong. In the case shown in Fig. 11, the maximum of the initial potential $\beta V_m=0.96$ and this rises to 2.6 as the island size increases. The important measure of the potential is given by the maximum Peclet number,[11] which should normally be <1 for good convergence. In the cases illustrated in Figs. 1 and 2 the Peclet number stays below 0.61 at all annealing times, but this is just under 5 times higher for Fig. 3. In these latter cases both methods are stable up to a Peclet number of $\sim$3, but the values obtained are slightly different. In particular it appears that the two methods approach the same answer from opposite directions, so that they effectively bracket the correct answer for all reasonable time steps Δt, as discussed in the text and Fig. 3.

The MATLAB®6.5 programs developed here have very short code, organized into a few (1–10) subroutines of typical size 1–10 kB. But the 2D moving picture file size can, depending on the mesh size and the number of frames kept, be anywhere upwards of 5 MB, and that is just for short presentations of typically 150 frames. So our current strategy is to keep only the programs, and not the 2D results, except in the immediate run-up to such presentations. This approach is possible because the calculations themselves take such a short time to run. No individual program result presented in this paper has taken more than 350 s, and most results have taken between 20 and 100 s, after optimizing the program specifically for that particular output. This contrasts with the major supercomputer calculations which are otherwise the norm in this field.

*Email address: john.venables@asu.edu

[1] J. A. Venables, Philos. Mag. **27**, 697 (1973), and references quoted; J. A. Venables, Phys. Rev. B **36**, 4153 (1987); Surf. Sci. **299**, 798 (1994); *Introduction to Surface and Thin Film Processes* (Cambridge University Press, Cambridge, 2000), especially Chap. 5.

[2] H. Brune, Surf. Sci. Rep. **31**, 121 (1998).

[3] J. Repp, F. Moresco, G. Meyer, K-H. Rieder, P. Hyldgaard, and M. Persson, Phys. Rev. Lett. **85**, 2981 (2000); N. Knorr, H. Brune, M. Epple, A. Hirstein, M. A. Schneider, and K. Kern, Phys. Rev. B **65**, 115420 (2002).

[4] A. Bogicevic, S. Ovesson, P. Hyldgaard, B. I. Lundqvist, H. Brune, and D. R. Jennison, Phys. Rev. Lett. **85**, 1910 (2000); S. Ovesson, A. Bogicevic, G. Wahnström, and B. I. Lundqvist, Phys. Rev. B **64**, 125423 (2001). See also Refs. 6 and 7 for more detailed comments.

[5] K. A. Fichthorn and M. Scheffler, Phys. Rev. Lett. **84**, 5371 (2000); K. A. Fichthorn, M. L. Merrick, and M. Scheffler, Appl. Phys. A: Mater. Sci. Process. **75**, 17 (2002).

[6] S. Ovesson, Phys. Rev. Lett. **88**, 116102 (2002).

[7] J. A. Venables and H. Brune, Phys. Rev. B **66**, 195404 (2002); for a shorter version, see J. A. Venables, H. Brune, and J. Drucker, in *Morphological and Compositional Evolution of Thin Films*, edited by N. Bartelt *et al.*, MRS Symposia Proceedings No. 749 (Materials Research Society, Warrendale, PA, 2003), p. 17.

[8] C. Ratsch and J. A. Venables, J. Vac. Sci. Technol. A **21**, S96 (2003).

[9] P. Yang and J. A. Venables, in *Modeling of Morphological Evolution at Surfaces and Interfaces*, edited by J. Evans, C. Orme, M. Asta, and Z. Zhang, MRS Symposia Proceedings No. 859E, (Materials Research Society, Warrendale, PA, 2005), JJ3.2.

[10] J. A. Venables and P. Yang, in *Modeling of Morphological Evolution at Surfaces and Interfaces*, edited by J. Evans, C. Orme, M. Asta, and Z. Zhang, MRS Symposia Proceedings No. 859E (Materials Research Society, Warrendale, PA, 2005), JJ9.2

[11] R. Grima and T. J. Newman, Phys. Rev. E **70**, 036703 (2004).

[12] G. S. Bales and D. C. Chrzan, Phys. Rev. B **50**, 6057 (1994).

[13] H. Brune, G. S. Bales, J. Jacobsen, C. Boragno, and K. Kern, Phys. Rev. B **60**, 5991 (1999).

[14] V. Halpern, J. Appl. Phys. **40**, 4627 (1969).

[15] M. J. Stowell, Philos. Mag. **26**, 349 (1972); **26**, 361 (1972).

[16] B. Lewis and G. J. Rees, Philos. Mag. **20**, 1253 (1974); B. Lewis

and J. C. Anderson, *Nucleation and Growth of Thin Films* (Academic Press, London, 1978), pp. 238–246.
[17] The Nernst-Einstein formulation is given in many places. For details, see comments and references in Sec. IV of Ref. 7.
[18] In Ref. 11, the same case is considered, but the velocity $\boldsymbol{v}(\boldsymbol{r}) = +\alpha\boldsymbol{\nabla}\phi(\boldsymbol{r})$, where $\phi(\boldsymbol{r})$ is a general scalar field. Here $\boldsymbol{v}(\boldsymbol{r})$ is directed down the potential gradient $\boldsymbol{\nabla}V(\boldsymbol{r})$.
[19] In Ref. 10, the hybrid-FFT method was applied with a locally varying average diffusion coefficient. But this does not conserve particles exactly in the presence of a potential, unlike the method proposed here, as explained in Appendix C.
[20] R. Grima, J. Degraffenreid, and J. A. Venables (unpublished).
[21] T. A. Witten and L. M. Sander, Phys. Rev. Lett. **47**, 1400 (1981); Phys. Rev. B **27**, 5686 (1983).
[22] T. Michely and J. Krug, *Islands, Mounds and Atoms* (Springer, Berlin, 2004), especially Chap. 3.
[23] There is a standard image solution of Laplace's equation, which shows that a hemispherical cap on a plane surface captures three times the flux as the same area without the hemisphere. For a semicircle on a line, the factor is 2; the first pixel on a side counts as two pixels for the flux.
[24] C. Ratsch, M. F. Gyure, S. Chen, M. Kang, and D. D. Vvedensky, Phys. Rev. B **61**, R10598 (2000).
[25] C. Ratsch, M. Kang, and R. E. Caflisch, Phys. Rev. E **64**, 020601(R) (2001).
[26] Z. He, D. J. Smith, and P. A. Bennett, Phys. Rev. Lett. **93**, 256102 (2004).
[27] A. Pradhan, N-Y. Ma, and F. Liu, Phys. Rev. B **70**, 193405 (2004).
[28] J. H. G. Owen, K. Miki, and D. R. Bowler, J. Mater. Sci., doi: 10.1007/s10853-006-0246-x (2006).
[29] This potential (Ref. 6) is of the form $V(r) = Ar/(1+Br^4)$, where A and B are constants. As employed here, with the maximum at the edge of the island determining B, there is a strong potential discontinuity across diagonal directions when only the x- or y-side potential is used.
[30] C. Ratsch, P. Smilauer, D. D. Vvedensky, and A. Zangwill, J. Phys. I **6**, 575 (1996).
[31] I. Daruka and A-L. Barabási, Phys. Rev. Lett. **79**, 3708 (1997).
[32] F. Liu, S. E. Davenport, H. M. Evans, and M. G. Lagally, Phys. Rev. Lett. **82**, 2528 (1999).
[33] L. Huang, F. Liu, and X. G. Gong, Phys. Rev. B **70**, 155320 (2004).
[34] L. Huang, F. Liu, G.-H. Lu, and X. G. Gong, Phys. Rev. Lett. **96**, 016103 (2006).
[35] J. Degraffenreid, N. Ma, F. Liu, and J. A. Venables (unpublished).
[36] M. McKay, J. A. Venables, and J. Drucker (unpublished).
[37] P. Yang, P. A. Bennett, and J. A. Venables (unpublished).
[38] R. J. LeVeque, *Numerical Methods for Conservation Laws* (Birkhauser, Basel, 1990).
[39] P. Wesseling, *An Introduction to Multigrid Methods* (R.T. Edwards, New York, 2004).